# Atomic Layer Deposition of Platinum Nanocatalysts onto Three-Dimensional Carbon Nanotube/Graphene Hybrid

Chien-Te Hsieh,* Yung-Ying Liu, Dong-Ying Tzou, and Wei-Yu Chen

Department of Chemical Engineering and Materials Science, Yuan Ze Fuel Cell Center, Yuan Ze University, Taoyuan 32003, Taiwan

ABSTRACT: Nanoparticulate platinum (Pt) has been well dispersed onto a three-dimensional carbon framework, consisting of carbon nanotubes (CNTs) and graphene oxide (GO) sheets, through an atomic layer deposition (ALD) route. One liquid-phase homogenizing process is capable of inserting a number of CNTs into the interspacing of GO sheets, forming the CNT#GO hybrid. Two types of ALD precursors, methylcyclopentadienyl-(trimethyl) platinum and oxygen were used to grow Pt deposits at 250 °C. The ALD cycle number acts as a key parameter in affecting the growth of Pt into the CNT#GO framework, showing growth rates of 0.054 nm cycle^{-1} and 0.00081 mg cm^{-2} cycle^{-1} for particle size and weight loading, respectively. The particle size of as-grown Pt deposits exhibits an increase from 2.27 to 12.32 nm within 50−200 ALD cycles. Single-stack cell test confirms the novel design of Pt catalyst electrodes with ultralow Pt loading displaying a superior catalytic activity, showing a promising feasibility for application in fuel cells.
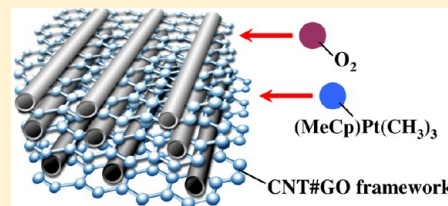
1. INTRODUCTION

Carbon supported electrocatalysts have been demonstrated in increasing the performance of proton exchange membrane fuel cells (PEMFCs) and decreasing the use of noble metals, traditionally Pt.[1] It is generally recognized that the design of catalyst electrodes not only raises the accessibility of nanosized catalyst surface area for electron transport but also provides better mass transport of reactants to electrocatalysts. As a result, pioneering efforts have been made in developing various carbon supports such as carbon black,[2] carbon nanotubes (CNTs),[3−6] carbon aerogels,[7] and so on. The target is to utilize these carbon supports as conductive carbon scaffold to attain high surface area available for the dispersion of metallic nanocatalysts. Recently, one two-dimensional carbon material, graphene nanosheet (GN), has emerged for use as carbon support in PEMFCs due to its unique morphology and superior electronic conductivity. The GNs prepared through the exfoliation of graphite leave behind some defects and vacancies, which serve as good anchoring sites for the deposition of metal nanoparticles, beneficial for the application of PEMFCs. However, because of van der Waals interaction, as-prepared GNs tend to form an aggregate (or restacking layers), making it difficult to express their intrinsic chemical and physical properties.

One strategy to resolve the above problem is adhering nanospacer to GNs, thus exfoliating the graphene agglomerate with high surface area. Basically, an ideal spacer is capable of intercalating uniform nanospacers, facilitating the rigidity of two-dimensional GNs. Advanced research achievements have been made by using zero-dimensional nanoparticles including Fe$_3$O$_4$,[8] Co$_3$O$_4$,[9] SnO$_2$,[10,11] Cu$_2$O,[12] and Si.[13,14] To date, one-dimensional CNTs have been taken into account to be the spacer into the graphene oxide (GO) sheets, generating a three-dimensional carbon framework. The hierarchical hybrid has been proved to improve the performance of electrochemical capacitors,[15,16] counter electrode for dye-sensitized solar cells,[17] and catalyst electrodes for methanol oxidation,[18] oxygen reduction reaction,[19−21] and accessible hydrogen-adsorbed surface area.[22]

This present work provides an efficient homogenizing method to prepare the three-dimensional hierarchical framework for diminishing the face-to-face aggregation of GO sheets. The stacking of individual GNs can be inhibited by inserting one-dimensional CNTs into two-dimensional GO sheets. To avoid the destruction of the carbon framework, one atomic layer deposition (ALD) route is adopted to uniformly disperse Pt nanoparticles onto the framework, forming the Pt-coated carbon hybrid. In fact, there has been increasing interest in applying ALD route to deposit Pt nanoparticles on TiO$_2$ catalysts,[23] mesoporous silica,[24] carbon aerogels,[25] and CNTs.[26] Because of its self-limiting nature of surface reactions, ALD can be used to control the amount of catalyst deposited on the carbon framework. Therefore, the ALD is ideally suited to prepare ultralow loading in gas diffusion electrodes with highly catalytic activity. The influence of ALD cycle on the Pt loading and particle size distribution are systematically investigated. In comparison with traditional chemical reduction, the ALD method takes some advantages such as particle uniformity (with narrow size distribution), easy to control Pt loading (via ALD cycle), and dry in/dry out process (without any waste liquid during ALD process). The merit of the present work is to develop a novel design of gas diffusion electrode that consists of CNT#GO carbon support and ALD-Pt catalysts, showing a feasibility for commercialization.
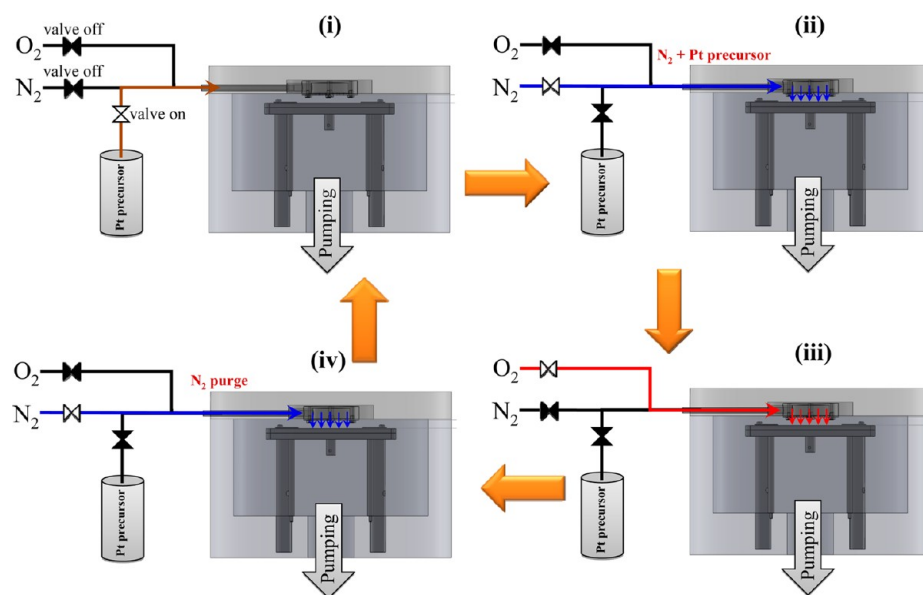
Figure 1. Layout of one ALD cycle for depositing Pt nanoparticles onto the carbon support, consisting of four steps: (i) 1 s MeCpPtMe₃ pulse, (ii) 5 s N₂ carrying, (iii) 2.5 s O₂ pulse, and (iv) 20 s N₂ purge.

2. EXPERIMENTAL METHODS

2.1. Preparation of CNT#GO Composites. The GO nanosheets were exfoliated from natural graphite (NG) powders with a mean size of 5 μm by a modified Hummers method as described previously.[27,28] In a typical synthesis, the NG powders were immersed in a solution with strong oxidizing agents (1 M $KMnO_4$ and concentrated H_2SO_4). The graphite slurry was then neutralized and subjected to several cycles of filtration and washing with distilled water. The GO powder was stored and dispersed in ethylene glycol (EG) solution. Similarly, multiwalled CNTs (commercial product) were also stored in EG solution after chemically oxidizing the CNTs in nitric acid at 90 °C for 3 h. Both carbon slurries containing GO sheets and CNTs (with weight ratio of 1:1) were mixed together, and the mixture was placed into a high-performance homogenizer (IKA, Model T25, Germany). The homogenizing dispersion process was carried out at ambient temperature for 30 min, allowing the formation of homogeneous CNT#GO composite. A spray method was adopted to coat the derived CNT#GO composite over carbon paper (CP) substrate (TGP-H, Toray Composites Inc., Japan). The substrate was composed of carbon fibers with an average diameter of 8−10 μm, and a thickness of 190 μm. The CNT#GO CP cake was then heated to 105 °C to evaporate the moisture, thus giving the desired CNT#GO/CP composite within a thickness of ca. 10 μm. The weight loading of CNT#GO on the CP substrate was approximately 0.8 mg cm^{-2} after the drying.

2.2. ALD of Pt on CNT#GO Composites. The CNT#GO CP hybrids were cut into an area of 2.5 × 2.5 cm^2, and the control of the exposure area depended on the further test of single-stack PEMFC (i.e., 5 cm^2). In the ALD of Pt catalysts, the Pt nanoparticles were grown on the CNT#GO supports by using (methylcyclopentadienyl) trimethylplatinum (MeCpPtMe₃, 99%) and high-purity oxygen (99.9995%) as ALD precursors. Prior to the ALD process, the O₂ gas was dried through a desiccant dryer to a dew point temperature of −45.5 °C, and the MeCpPtMe₃ was kept at 60 °C. An ultrahigh-purity N₂ (99.9995%) was used as carrier and purging gases. The regular ALD cycle consisted of (i) 1 s exposure to

MeCpPtMe₃, (ii) 5 s N₂ carrying out of MeCpPtMe₃, (iii) 2.5 s exposure to O₂, and (iv) 20 s N₂ purge, as shown Figure 1. In step (ii), the N₂ served as a carrier to carry the gaseous mixture (i.e., MeCpPtMe₃ + N₂) in the support substrate. In the ALD design, the nitrogen carrying step (step (ii)) was capable of (i) cleaning the gas delivery lines and (ii) carrying the Pt precursor, ensuring the whole penetration of MeCpPtMe₃ in the carbon framework, as shown in Figure 1a,b. The continuously pumping step was used to remove any unreacted precursors from the sample substrate and the gas delivery line. The Pt nanoparticles were deposited with the support temperature at 250 °C at a reactor pressure of 700 mTorr after 50, 100, 200, and 400 ALD cycles. The schematic illustration for growing the ALD-Pt nanoparticles deposited on the surface of CNT#GO hybrid could be depicted in Figure 2.

2.3. Characterization of ALD-Pt Catalysts. Field-emission scanning electron spectroscope (FE-SEM, JEOL JSM-5600) and high-resolution transmission electron microscope (HR-TEM, JEOL, JEM-2100) were adopted to observe the topography and distribution of ALD-Pt nanoparticles on the CNT#CP hybrids. An automated adsorption apparatus (Micromeritics, ASAP 2020) was employed for analyzing the surface characteristics of the carbon samples (i.e., fresh GO sheets, CNTs and CNT#GO composite), using N₂ phys-isorption at −196 °C. Specific surface areas and pore size distributions of the carbons were evaluated with the application of the Brunauer−Emmett−Teller (BET) and the Barrett−Joyner−Halenda (BJH) equations, respectively. A thermogravimetric analyzer (TGA, Perkin-Elmer TA7) was used to analyze the amount of ALD-Pt catalysts deposited on the carbon composites. The Pt-loaded carbon composite was carefully cut into an area of 1 cm^2 and then placed in the TGA. The sample was heated to 900 °C at a heating rate of 10 °C/min in air atmosphere, thus getting the residual metallic content. To ensure the accuracy of the Pt loading, the TGA analysis was conducted for each sample twice. The crystalline structure of the ALD-Pt catalysts was examined by grazing incident X-ray diffraction (XRD) with Cu−Kα radiation, using an automated X-ray diffractometer (Rigaku, D/MAX 2500). The chemical
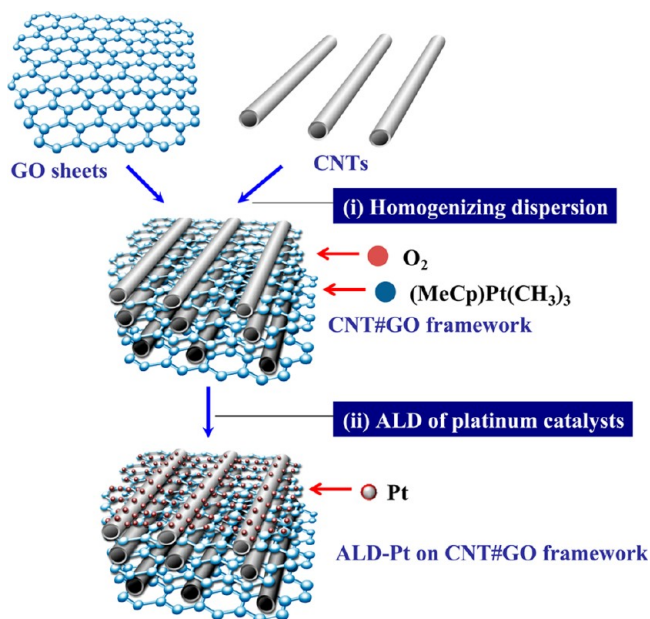
Figure 2. Schematic diagram for preparing the Pt nanoparticles deposited on the surface of CNT#GO hybrids, involving (i) homogenizing dispersion and (ii) ALD of Pt catalysts.

composition and functional group distribution of the carbon samples were analyzed using X-ray photoelectron spectroscopy (XPS). The XP spectra were recorded with a Fison VG ESCA210 spectrometer and Mg Kα radiation. The deconvolution of the spectra was carried out using a nonlinear least-squares fitting program with a symmetric Gaussian function.

2.4. Performance Test of a Single Cell. The membrane electrode assembly (MEA) was first fabricated to study the performance of a single cell, using the ALD-Pt electrode as the anode, the Nafion 212 layer (Dupont Inc.) as the proton exchange membrane, and a commercial gas diffusion electrode (10 wt % Pt/C, 0.40 mg cm^{-2}, Johnson Matthey) as the cathode. The ALD-Pt catalyst electrode was painted with 5 wt % Nafion 212 solution to obtain a Nafion loading of 0.6 mg cm^{-2} on the electrode. The Nafion-impregnated electrodes and membrane were then hot pressed together at 135 °C for 1 min at a pressure of 40 atm, forming the MEA. Subsequently, the MEA was inserted between two graphite plates with a serpentine flow pattern. The performance test was conducted using a 5 cm^2 single fuel cell operated at 30, 45, 60, and 75 °C. High-purity hydrogen (99.999%) and oxygen (99.999%) were fed at the anode and cathode, respectively, both at flow rates of 200 cm^3 min^{-1} at 100% relative humidity. The polarization curve and the power density of the single cell were then monitored and characterized.

3. RESULTS AND DISCUSSION

The surface morphology of fresh GO sheets and CNTs was examined by HR-TEM observation, as shown in Figure 3a,b. These images clearly depict that the as-prepared GO sheets display a two-dimensional layered structure, whereas the CNTs
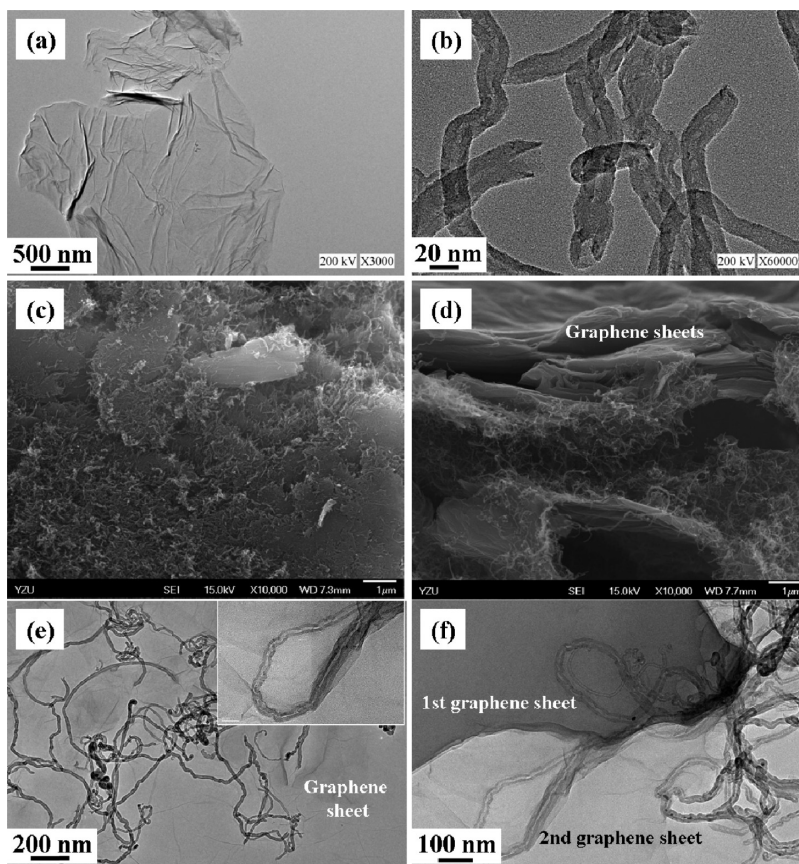

Figure 3. HR-TEM images of (a) fresh GO sheets and (b) blank CNTs. (c) Tilt and cross-sectional views of FE-SEM micrographs of CNT#GO hybrids through a homogenizing dispersion route. HR-TEM images of the CNT/GO hybrids with (e) low and (f) high magnifications, showing a number of CNTs inserted into the interspacing GO sheets. The inset of panel e shows single CNT inserted between GO sheets.

exhibit a one-dimensional tubular form. The GO sheets look transparent and are of multilayers with an area of a few micrometers. The CNTs show a uniform distribution in tube diameters from 20 to 40 nm. After the homogenizing dispersion, a large number of nanotubes are inserted into the interspacing of GO sheets, forming a three-dimensional framework, as shown in cross-sectional views of FE-SEM images (see Figure 3c,d). Since the tangled CNTs protrude out of the graphene sheets, it can be suggested that the framework is rough enough for use as an electrocatalyst support. To inspect the observation, Figure 3e,f presents HR-TEM images of CNT#GO hybrids with low and high magnifications, respectively. It can be seen that the nanotubes are attached to the graphene sheets, and some of coiled tubes tend to aggregate together and thus form a network in the GO interlayer. The inset of Figure 3e confirms the formation of stereo CNT#GO framework, showing that one individual CNT is inserted between the GO sheets. The sandwich structure, consisting of the intercalation of CNTs into the layered GO sheets, confirms that the homogenizing process is capable of well inserting the CNTs into GO sheets.

Table 1 shows the porous characteristics of different carbon samples, determined from the data of the adsorption isotherms.

Table 1. Surface Characteristics of Carbon Materials Determined from Nitrogen Physisorption at −196 °C

carbon type	O/C atomic ratio[a] (%)	S_{BET}[b] (m²/g)	V_t[c] (cm³/g)	mean pore size[d] (nm)
CNT	8.8	115.2	0.37	14.8
GO	47.7	10.1	0.04	10.1
CNT#GO	31.5	313.3	1.13	17.5

[a]O/C atomic ratio: atomic ratio determined from the XPS analysis. [b]S_{BET}: specific surface area computed using the BET equation. [c]V_t: total pore volume estimated at a relative pressure of 0.98. [d]Mean pore size: mean pore size determined from the BJH model.

For comparison, the CNT#GO hybrid displays a BET surface area of 313.3 m²/g, which is higher than GO sheets and CNTs with low surface areas of 10.1 and 115.2 m²/g, respectively. The pore structures of all carbons are mainly mesoporous because of their high mesopore volumes, determined by the BJH equation (i.e., the pore size between 2 and 50 nm, defined by the IUPAC classification). The enhanced porosity in the CNT#GO hybrid can be attributed to the fact that some GO sheets in the framework are effectively exfoliated into nanosheets with wrinkles, preventing them from the restacking aggregation. Thus, the stereo framework, incorporated with CNTs and GO sheets, provides more voids and cavities available for N_2 adsorption. Since all carbons are mainly mesoporous, the BJH method was adopted to analyze the mesopore size distribution, as depicted in Figure 4. This figure reveals that these carbon samples exhibit different pore size distributions: (i) the GO sheets with two lumps at pore sizes 2−3 and 8−10 nm and (ii) the CNTs with three lumps at 3−5, 8−10, and 20−40 nm. The porosity in the CNTs possibly originates from inner cavities, interstitial channels, both ends, ridges, and the aggregate's outer surfaces. In contrast, the CNT#GO composite exhibits a similar topography in the pore size distribution to the CNTs. Obviously, the original distribution of GO sheets disappears after the introduction of CNTs. It has shown that the hybrid creates a large number of surface areas within mesopore range of 10−100 nm, indicating the intercalation of
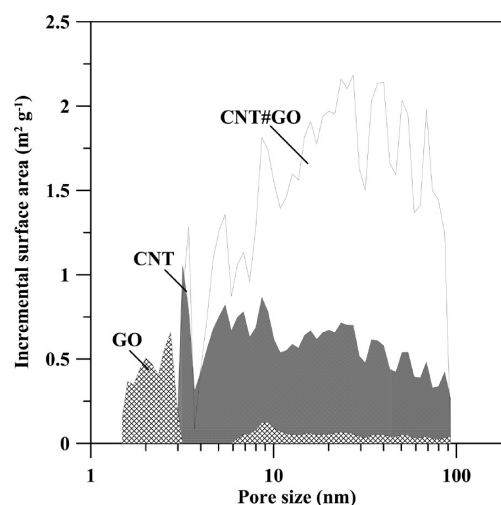

Figure 4. Pore size distributions of GO sheets, CNTs, and CNT#GO hybrid, determined by the BJH method.

CNTs (having an average diameter of 20−40 nm) into the GO stacking layers. This result confirms that the insertion of CNTs between the GO sheets shows the positive effect on the improvement of surface porosity.

XPS was adopted to examine the oxidation level and the distribution of oxygen functionalities on the CNT#GO framework. A quantitative analysis was performed to evaluate the O/C atomic ratios, wherein the C 1s and O 1s peaks of the scan spectra have binding energies of ca. 284.6 and 533.5 eV, respectively.[29] Quantitative analysis was applied to evaluate the surface C and O concentrations, showing the (O 1s)/(C 1s) ratio of 31.5% in the CNT#GO hybrid (see Table 1). For comparison, the (O 1s)/(C 1s) ratios of GO sheets and CNTs are found to have 47.7 and 8.8%, respectively. As depicted in Figure 5, the C 1s peak has been deconvoluted using a peak
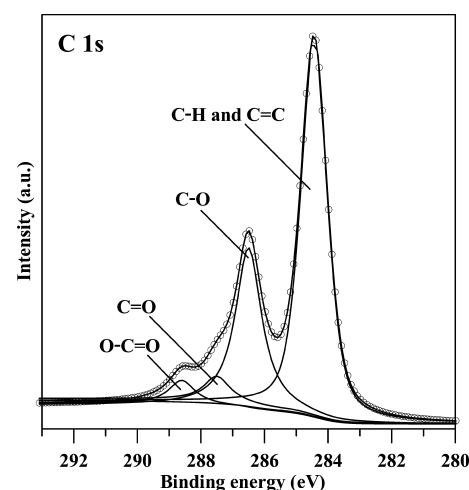

Figure 5. XPS C 1s spectrum of as-prepared CNT#GO hybrids, deconvoluted by a multiple Gaussian function.

synthesis procedure in which a Gaussian peak shape was assumed to fit each component with a fixed binding energy. These binding energy peaks have been identified as sp² carbon at 284.6 eV, C−O at 286.7 eV, C=O at 288.4 eV, and O−C= O at 289.7 eV.[30−33] The results of XPS analysis proves that the as-received CNT#GO hybrid possesses a highly oxidized
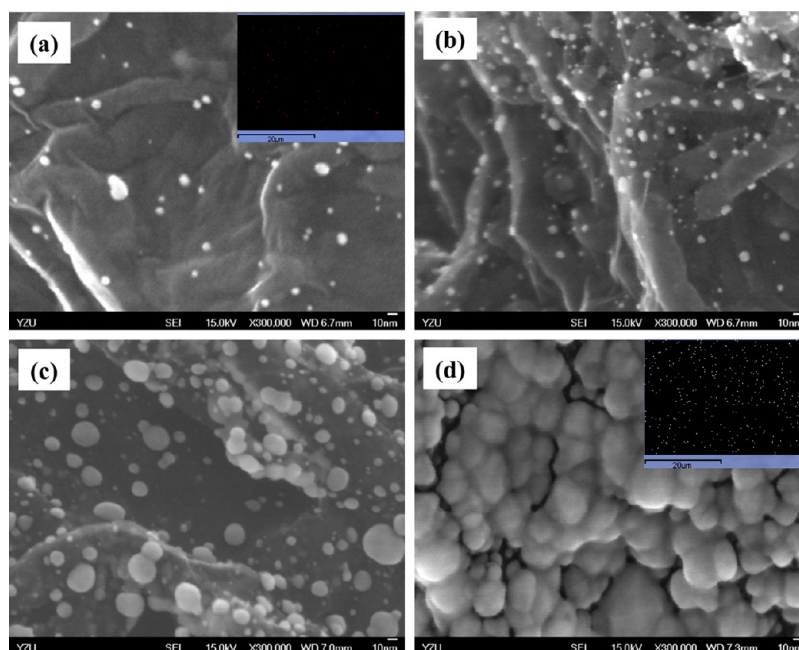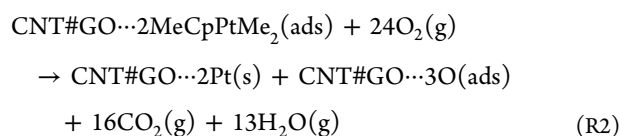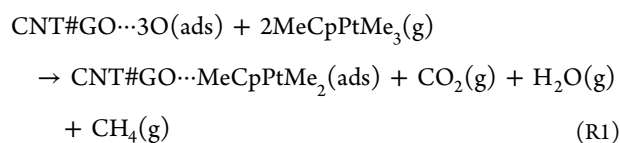
Figure 6. Top-view FE-SEM photographs of as-grown Pt catalysts onto CNT#GO hybrids prepared by ALD route: (a) 50, (b) 100, (c) 200, and (d) 400 cycles. The insets of panels a and d show the Pt mapping over the surface of CNT#GO composite after 50 and 400 cycles, respectively.

surface, occupied by oxygen functionalities including hydroxyl, carbonyl, and carboxylic groups. As a result, the CNT#GO hybrid exhibits a stereostructure with a large number of oxygen functional groups bearing basal planes, defects, and edges.[30,34]

Figure 6 shows the top-view FE-SEM images of the resultant ALD-Pt catalysts on the surface of CNT#GO composites with different ALD cycles, ranged from 50 to 400 cycles. The insets of Figure 6a,d show the mapping of ALD-Pt nanoparticles after 50 and 400 cycles, proving well-dispersed nanodots over the surface of CNT#GO hybrids. The Pt particles appear as various morphologies over the surface of GO sheets due to different ALD cycles. Within the ALD cycles of 50−200 cycles, the as-grown Pt is randomly deposited over the top layer of GO sheets. After 200 cycles, the Pt deposit tends to merge with neighboring Pt, forming a continuous layer. Generally, the density of Pt deposits is an increasing function of the ALD cycles, confirming the presence of self-limiting surface reaction. It is generally recognized that the oxygen functionalities play the key role in affecting the distribution of Pt monolayer through self-limiting reactions.[26]

In the synthesis of ALD, these oxide groups are expected to act as active sites for chemically adsorbing with Pt precursors (i.e., $MeCpPtMe_3$) in gas phase, thus forming the first atomic Pt monolayer. The mechanism for growing the atomic layer can be expressed as two self-limiting reactions:[35]

$$CNT\#GO\cdots3O(ads) + 2MeCpPtMe_3(g)$$
$$\rightarrow CNT\#GO\cdots MeCpPtMe_2(ads) + CO_2(g) + H_2O(g)$$
$$+ CH_4(g) \tag{R1}$$

$$CNT\#GO\cdots2MeCpPtMe_2(ads) + 24O_2(g)$$
$$\rightarrow CNT\#GO\cdots2Pt(s) + CNT\#GO\cdots3O(ads)$$
$$+ 16CO_2(g) + 13H_2O(g) \tag{R2}$$

where CNT#GO···3O and CNT#GO···2Pt represent the active sites occupied by oxide functionalities and the ALD-Pt atomic layer, respectively. Basically, one ALD cycle consists of four steps including (i) $MeCpPtMe_3$ pulse, (ii) system purge, (iii) oxygen pulse, and (iv) system purge. The first self-limiting reaction R1 takes place in steps (i) and (ii), whereas the second one R2 occurs in steps (iii) and (iv). It is believed that (i) the self-limiting reactions are instantaneous and (ii) the CNT#GO···3O sites almost cover the surface of as-grown Pt nanoparticles after the first ALD cycle. The oxygenated layer is capable of providing a number of active sites to induce the sequent deposition of Pt nuclei, i.e., a layer-by-layer atomic growth. It is generally recognized that the diffusion rate is strongly affected by the porosity of carbon support and the diffusion path. From the data in Table 1, one can see that the CNT#GO framework possesses high BET surface and vast mesoporosity, allowing the fast diffusion of Pt precursor. Because of the limiting reaction steps, the amount of Pt nanoparticles into the CNT#GO hybrids tends to increase with ALD cycle number.

Figure 7 shows FE-SEM photographs of as-grown Pt catalysts (ALD cycle, 200) onto CNT#GO hybrids focusing on the edge of CNT#GO layer and the CNT forest, respectively. It can be seen that the Pt nanoparticles are dispersed over the surface of CNT#GO layers with good uniformity, i.e., from bottom to top layer. The well-dispersed Pt nanoparticles are also found in the CNT forest, in where the nanoparticles are uniformly decorated with the surface of CNTs. This finding confirms that the gaseous precursors (i.e., $MeCpPtMe_3$ and O_2 in this case) can easily penetrate through the carbon framework without strong diffusion resistance, thus forming well dispersion of ALD-Pt nanoparticles over the carbon hybrid. On the basis of the results, the influence of diffusion resistance on the uniformity of ALD-Pt catalysts seems to be minor, and the ALD route shows a great ability to grow uniform Pt in the unique framework under the operating conditions.
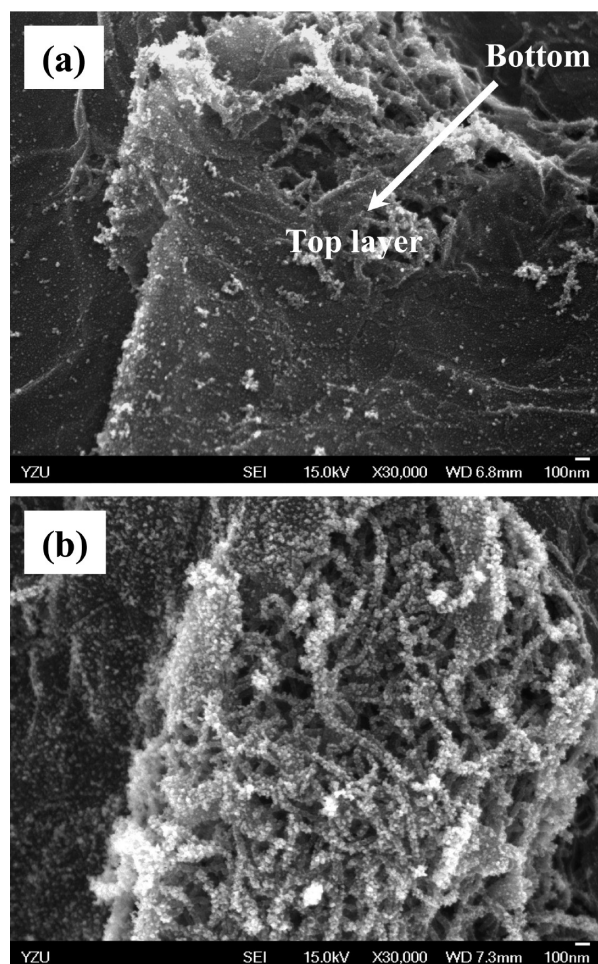
26739

dx.doi.org/10.1021/jp303552j | J. Phys. Chem. C 2012, 116, 26735−26743

Figure 7. FE-SEM photographs of as-grown Pt catalysts (ALD cycle, 200) onto CNT#GO hybrids focusing on (a) the edge of CNT#GO layer and (b) the CNT forest.

Typical XRD patterns of the resulting ALD-Pt nanoparticles over the CNT#GO hybrids are collected in Figure 8, showing the presence of face-centered cubic (fcc) Pt crystal. The
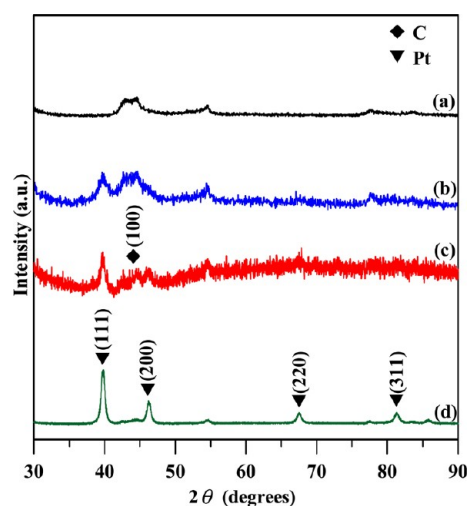

Figure 8. Typical XRD patterns of as-grown Pt nanoparticles on the surface of CNT#GO hybrids prepared by ALD route: (a) 50, (b) 100, (c) 200, and (d) 400 cycles.

representative diffraction peaks appear at 39.8°, 46.2°, and 67.5°, corresponding to Pt(111), (200), and (220), respectively. When ALD cycle is less than 100, almost no obvious peaks can be observed, originating from ultralow Pt loading. Generally, the intensities of the representative peaks are increased by the ALD cycle, implying an increase in crystalline Pt loading. The Pt grains are found to exhibit the (111) plane with the highest intensity, indicating that the growth of Pt nanoparticles favors a preferential crystallographic direction (i.e., Pt(111) plane), i.e., an anisotropic growth of Pt crystals.

The dispersion of ALD-Pt deposits can be investigated in Figure 9; it shows the HR-TEM images of the resulting Pt onto CNT#GO hybrids through the ALD synthesis after 50, 100, and 200 cycles. The images clearly reveal that these Pt particles display different dispersion levels after different ALD cycles, confirming the importance of ALD cycles on affecting the dispersion. Additionally, the ALD process allows not only the attachment of Pt to the surface of GO sheets but also the deposition over the surface of CNTs. The selected-area electron diffraction from an area focusing on the ALD-Pt nanoparticles is shown in the inset of Figure 9a, indicating the presence of bright diffraction spots along with diffraction rings. Such rings confirm the formation of polycrystalline Pt onto the surface of CNT#GO hybrid after the ALD process. The particle-size distributions of Pt particles over the carbon hybrids after 50, 100, and 200 cycles are illustrated in the right side of Figure 9. The statistical results were obtained from counting ca. 100 ALD-Pt particles within a fixed observable area. As it can be seen, the Pt particles at 50 ALD cycles exhibit a homogeneous dispersion with a narrow distribution, while a very broad distribution appears after 200 cycles. The mean particles size shows an order as follows: 2.27 nm (50 cycles) < 3.95 nm (100 cycles) < 12.32 nm (200 cycles).

The variation of mean particle size with the ALD cycles can be clarified, as shown in Figure 10. It can be seen that the linear growth particle size with ALD cycle, reflecting a growth rate of 0.054 nm cycle^{-1} for the Pt deposits into the CNT#GO framework. In addition, an increasing trend of Pt loading rate with the cycle can be divided into two regions: 50−200 cycles (0.00081 mg cm^{-2} cycle^{-1}) and 200−400 cycles (0.00025 mg cm^{-2} cycle^{-1}). The growth rate of Pt loading after 200 cycles becomes slow, possibly resulting from the completion of Pt nuclei monolayer over the surface of carbon hybrid. At high ALD cycle, the interaction among the neighboring Pt nuclei tends to dominate the ALD process. Thus, the nuclei gradually start to merge, inducing the formation of Pt islands and a continuous layer. Because of different surface interactions between Pt−C and Pt−Pt bonds, the phenomena mentioned above affect the growth rate of Pt deposits during the ALD process. Such high loading of Pt deposits (i.e., > 200 ALD cycles) would limit the practical PEMFC application due to low catalytic activity and excessive cost.

The performance of catalyst electrode in a single-stack PEMFC operated at different temperatures from 30 to 75 °C was investigated, as shown in Figure 11. The polarization curves were obtained from a single cell in which ALD-Pt and commercial Pt electrode (0.40 mg cm^{-2}) served as anode and cathode, respectively. Herein, the ALD-Pt loadings in the anodes after 50 and 100 cycles are 0.061 and 0.13 mg cm^{-2}, respectively. It can be proposed that the hydrogen oxidation reaction (HOR) in the anode could be the rate-determining step since the Pt catalyst loading in the cathode is three times higher than the ALD-Pt loading in the anode. As the curves
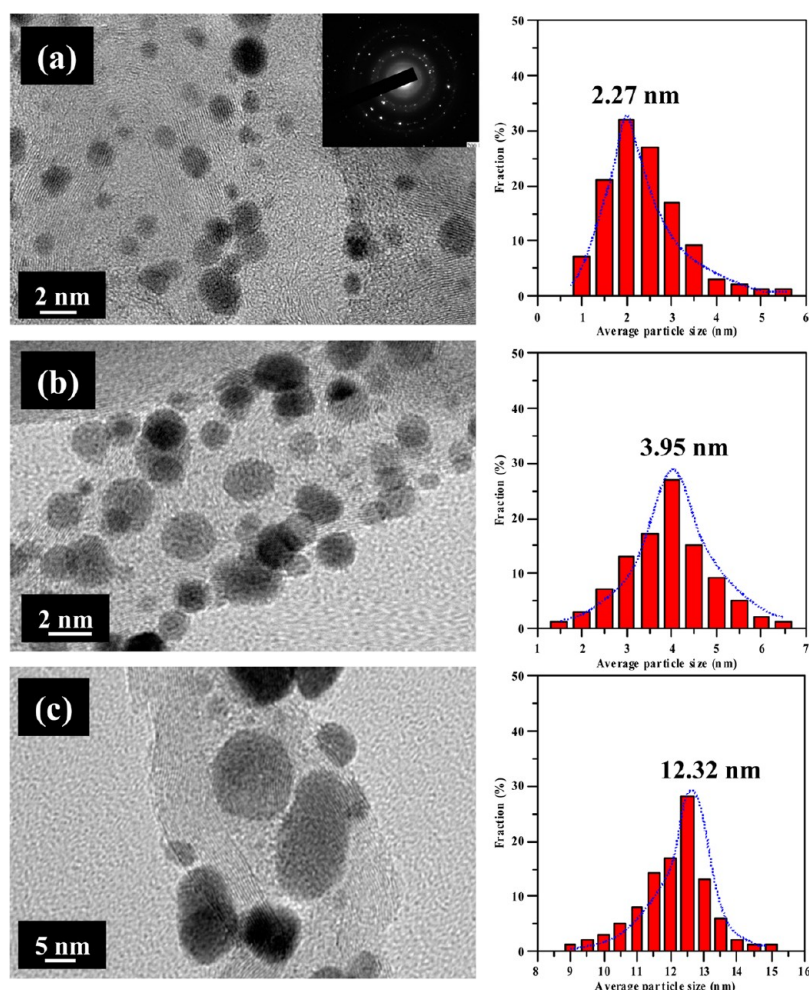
Figure 9. HR-TEM images of as-grown Pt nanoparticles on the surface of CNT#GO hybrids prepared by ALD route after (a) 50, (b) 100, and (c) 200 cycles. The right-side pictures correspond to their particle size distributions. The inset of panel a shows the SAD pattern focusing on ALD-Pt nanoparticles.
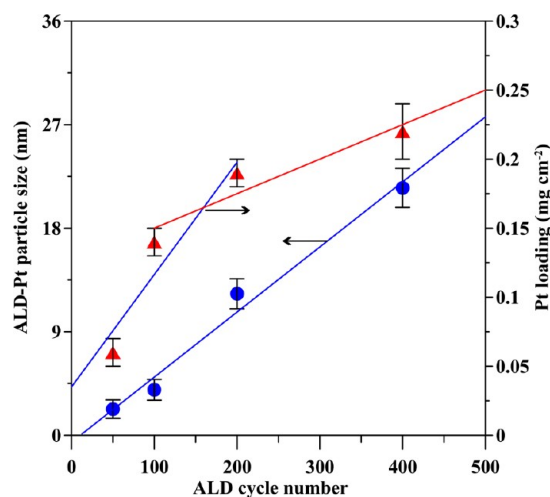

Figure 10. As-grown Pt particle size and weight loading as a function of ALD cycle.

show, both MEAs show an increasing peak power density with increasing cell temperature. The improved performance is mainly attributed to the following explanations: (i) the catalytic activity of HOR increases with increasing cell temperature, thus reducing the effect of activation polarization; (ii) the ionic

conductivity of Nafion membrane or Nafion ionomer in the catalyst layer is promoted with increasing cell temperature; and (iii) both reactant diffusion and product removal increase at high operating temperature, leading to faster redox kinetics.[36]

The peak power density of ALD-Pt catalysts varied with operating temperatures, as illustrated in Figure 12. It is reasonable that the maximal power density appears at 75 °C, i.e., 1.15 and 2.32 kW g^{-1} for 50 and 100 cycles, respectively. For comparison, the Pt catalyst at ALD 100 cycles displays the better cell performance than at 50 cycles within the temperature region. Since both ALD-Pt catalysts show small particle sizes of 2.27−3.95 nm, the influence of catalyst size on the cell performance seems to be minor. This difference can be ascribed to the dispersion and loading of Pt deposits. In the CNT#GO framework, the Pt nanoparticles attached to CNTs and GO sheets generate a number of catalytic sites, and the carbon support offers gas-diffusion channels and charge-transfer paths. However, the band gap of GO sheets generally increases with an increase of the O/C ratio, making the change of the band structure from a zero-gap to a finite-gap semiconductor.[37] Since the GO sheets possess a high oxidation level, this implies that the presence of GO sheets in the framework would restrict the charge transfer, thus raising the inner resistance of MEAs. As illustrated in the self-limiting steps (i.e., R1 and R2), the deposition of Pt atomic layer is significantly affected by the
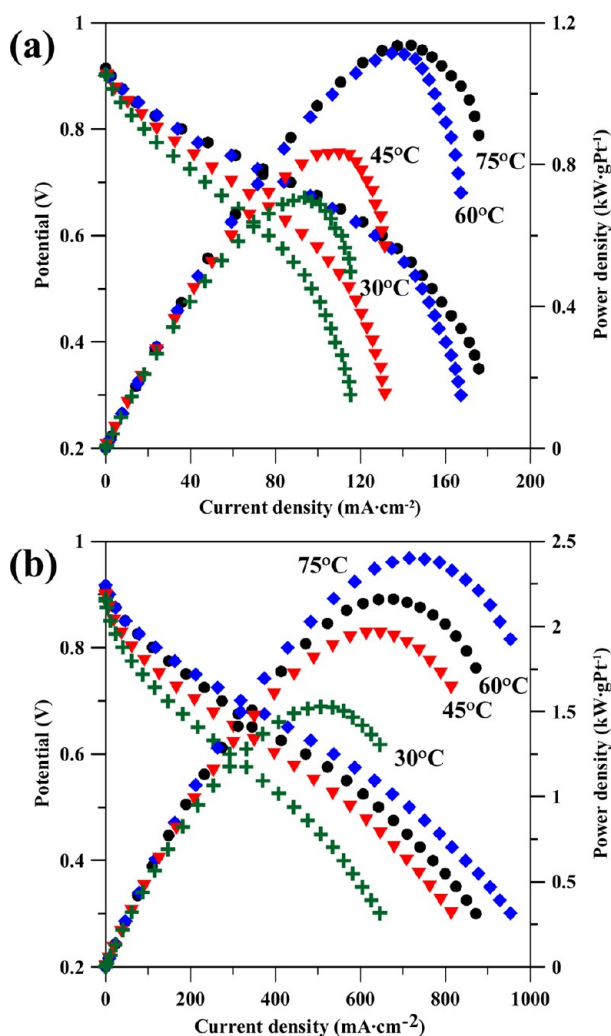
Figure 11. Performance curves obtained with MEAs equipped with ALD-Pt catalyst electrodes after (a) 50 and (b) 100 cycles at 30, 45, 60, and 75 °C.
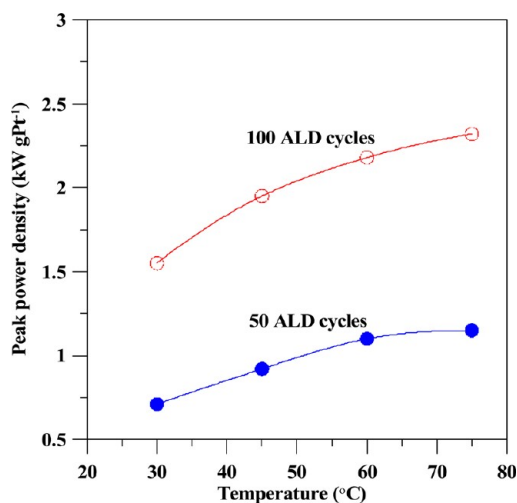

Figure 12. Peak power density of ALD-Pt catalyst electrodes as a function of operating temperature.

distribution of surface oxides. A high density of Pt nanoparticles reflects high occupancy of O-containing sites on the GO sheets, allowing the smooth pathway for electron conduction. This can

be used to support the argument why high Pt loading would enhance the charge-transfer resistance of CNT#GO hybrids. On the basis of the above deduction, the ALD technique shows the commercial feasibility to synthesize Pt catalysts on CNT#GO hybrids, exhibiting high catalytic activity and low inner resistance for PEMFC application. However, an optimal ALD parameter setting incorporated with the reduced GO sheets are essential for improving the cell performance in the future.

4. CONCLUSIONS

The present work has demonstrated that Pt nanoparticles can be uniformly deposited onto the CNT#GO framework, prepared by a homogenizing dispersion process. The homogenizing method enabled the intercalation of CNTs into the interspacing of GO sheets in liquid phase, forming the CNT#GO hybrid. The ALD cycle number was selected as a crucial parameter in controlling the dispersion and the loading of Pt onto the carbon hybrid. The particle size of as-grown Pt deposits was found to have an increase from 2.27 to 12.32 nm within 50−200 ALD cycles. The increasing trend of the growth rate with the ALD cycle number reflected that the deposition rates of 0.054 nm cycle^{-1} and 0.00081 mg cm^{-2} cycle^{-1} for particle size and weight loading, respectively. One growth mechanism involving two self-limiting reactions was proposed to clarify the deposition of Pt nanoparticles over the support. The results of single-stack cell test showed that the novel design of ALD-Pt catalyst electrodes offers an improved catalytic activity. The ALD-Pt loading onto the hybrid was found to affect the cell performance, possibly resulting from high occupancy of O-containing sites by the atomic Pt particles, thus leading to high catalytic activity and low inner resistance. On the basis of the results, the ALD technique exhibits a great potential for depositing ultralow Pt loading onto the CNT#GO hybrids for PEMFC application.

■ AUTHOR INFORMATION

Corresponding Author

*Tel: 886-3-4638800, ext. 2577. Fax: 886-3-4559373. E-mail: cthsieh@saturn.yzu.edu.tw.

Notes

The authors declare no competing financial interest.

■ REFERENCES

(1) Seger, B.; Kamat, P. V. *J. Phys. Chem. C* **2009**, *113*, 7990−7995.
(2) Liu, Z.; Ling, X. Y.; Su, X.; Lee, J. Y. *J. Phys. Chem. B* **2004**, *108*, 8234−8240.
(3) Han, D. M.; Guo, Z. P.; Zeng, R.; Kim, C. J.; Meng, Y. Z.; Liu, H. K. *Int. J. Hydrogen Energy* **2009**, *34*, 2426−2634.
(4) Chen, W.; Zhao, J.; Lee, J. Y.; Liu, Z. *Mater. Chem. Phys.* **2005**, *91*, 124−129.
(5) Hsieh, C. T.; Lin, J. Y.; Wei, J. L. *Int. J. Hydrogen Energy* **2009**, *34*, 685−693.
(6) Chen, Z.; Higgins, D.; Tao, H.; Hsu, R. S.; Chen, Z. *J. Phys. Chem. C* **2009**, *113*, 21008−21013.
(7) King, J. S.; Wittstock, A.; Biener, J.; Kucheyev, S. O.; Wang, Y. M.; Baumann, T. F.; Giri, S. K.; Hamza, A. V.; Baeumer, M.; Bent, S. F. *Nano Lett.* **2008**, *8*, 2405−2409.

26742

dx.doi.org/10.1021/jp303552j | *J. Phys. Chem. C* 2012, 116, 26735−26743

(8) Lian, P.; Zhu, X.; Xiang, H.; Li, Z.; Yang, W.; Wang, H. *Electrochim. Acta* **2010**, *56*, 834−840.

(9) Kim, H.; Seo, D. H.; Kim, S. W.; Kim, J.; Kang, K. *Carbon* **2011**, *49*, 326−332.

(10) Paek, S. M.; Yoo, E. J.; Honma, I. *Nano Lett.* **2009**, *9*, 72−75.

(11) Wang, X. Y.; Zhou, X. F.; Yao, K.; Zhang, J. G.; Liu, Z. P. *Carbon* **2011**, *49*, 133−139.

(12) Xu, C.; Wang, X.; Yang, L.; Wu, Y. *J. Solid State Chem.* **2009**, *182*, 2486−2490.

(13) Wang, J. Z.; Zhong, C.; Chou, S. L.; Liu, H. K. *Electrochem. Commun.* **2010**, *12*, 1467−1470.

(14) Xiang, H.; Zhang, K.; Ji, G.; Lee, J. Y.; Zou, C.; Chen, X.; Wu, J. *Carbon* **2011**, *49*, 1787−1796.

(15) Yang, S. Y.; Chang, K. H.; Tien, H. W.; Lee, Y. F.; Li, S. M.; Wang, Y. S.; Wang, J. Y.; Ma, C. C. M.; Hu, C. C. *J. Mater. Chem.* **2011**, *21*, 2374−2380.

(16) Yu, D.; Dai, L. *J. Phys. Chem. Lett.* **2010**, *1*, 467−470.

(17) Battumur, T.; Mujawar, S. H.; Truong, Q. T.; Ambade, S. B.; Lee, D. S.; Lee, W.; Han, S. H.; Lee, S. H. *Curr. Appl. Phys.* **2011**, *12*, e49−e53.

(18) Jha, N.; Jafri, R. I.; Rajalakshmi, N.; Ramaprabhu, S. *Int. J. Hydrogen Energy* **2011**, *36*, 7284−7290.

(19) Yang, S. Y.; Chang, K. H.; Lee, Y. F.; Ma, C. C. M.; Hu, C. C. *Electrochem. Commun.* **2010**, *12*, 1206−1209.

(20) Arbizzani, C.; Righi, S.; Soavi, F.; Mastragostino, M. *Int. J. Hydrogen Energy* **2011**, *36*, 5038−5046.

(21) Ma, Y.; Sun, L.; Huang, W.; Zhang, L.; Zhao, J.; Fan, Q.; Huang, W. *J. Phys. Chem. C* **2011**, *115*, 24592−24597.

(22) Yang, S. Y.; Chang, K. H.; Lee, Y. F.; Ma, C. C. M.; Hu, C. C. *Electrochem. Commun.* **2010**, *12*, 1206−1209.

(23) Zhou, Y.; King, D. M.; Liang, X. H.; Li, J. H.; Weimer, A. W. *Appl. Catal., B* **2010**, *101*, 54−60.

(24) Li, J. H.; Liang, X. H.; King, D. M.; Jiang, Y. B.; Weimer, A. W. *Appl. Catal., B* **2010**, *97*, 220−226.

(25) King, J. S.; Wittstock, A.; Biener, J.; Kucheyev, S. O.; Wang, Y. M.; Baumann, T. F.; Giri, S. K.; Hamza, A. V.; Baeumer, M.; Bent, S. F. *Nano Lett.* **2008**, *8*, 2405−2409.

(26) Liu, C.; Wang, C. C.; Kei, C. C.; Hsueh, Y. C.; Perng, T. P. *Small* **2009**, *5*, 1535−1538.

(27) Hummers, W. S.; Offeman, R. E. *J. Am. Chem. Soc.* **1958**, *80*, 1339.

(28) Zhou, X.; Huang, X.; Qi, X.; Wu, S.; Xue, C.; Boey, F. Y. C.; Yan, Q.; Chen, P.; Zhang, H. *J. Phys. Chem. C* **2009**, *113*, 10842−10846.

(29) Wagner, C. D.; Riggs, W. M.; Davis, L. E.; Moulder, J. F.; Muilenberg, G. E. *Handbook of X-Ray Photoelectron Spectroscopy*; Perkin-Elmer Corp.: Eden Prarie, MN, 1979.

(30) Lee, W. H.; Kim, J. Y.; Ko, Y. K.; Reucroft, P. J.; Zondlo, J. W. *Appl. Surf. Sci.* **1999**, *141*, 107−113.

(31) Lee, W. H.; Reucroft, P. J. *Carbon* **1999**, *37*, 7−14.

(32) Takahagi, T.; Ishitani, A. *Carbon* **1984**, *22*, 43−46.

(33) Hsieh, C. T.; Teng, H.; Chen, W. Y.; Cheng, Y. S. *Carbon* **2010**, *48*, 4219−4229.

(34) Chen, S.; Zhu, J.; Wu, X.; Han, Q.; Wang, X. *ACS Nano* **2010**, *4*, 2822−2830.

(35) Kessels, W. M. M.; Knoops, H. C. M.; Dielissen, S. A. F.; Mackus, A. J. M.; van de Sanden, M. C. M. *Appl. Phys. Lett.* **2009**, *95*, 03114.

(36) Chen, S.; Ye, F.; Lin, W. *Int. J. Hydrogen Energy* **2010**, *35*, 8225−8233.

(37) Ito, J.; Nakamura, J.; Natori, A. S. *J. Appl. Phys.* **2008**, *103*, 113712−113715.